Electronic Supplementary Information

Hierarchical NiO-In_2O_3 Microflower (3D)/ Nanorod(1D) Hetero-Architecture as a High Performance Supercapacitor Electrode with Excellent Cyclic Stability

N. Padmanathan,[a] Han Shao[a,b], David Mcnulty[b], Colm O'Dwyer[a,b] and Kafil. M. Razeeb[a]*

[a] Tyndall National Institute, University College Cork, Dyke Parade, Lee Maltings, Cork, Ireland.

[b] Department of Chemistry, University College Cork, Cork, Ireland.

***Corresponding Author:**

Dr. Kafil M. Razeeb, Nano-Interconnection, Tyndall National Institute, University College Cork, Dyke Parade, Lee Maltings, Cork, Ireland. Phone: +353 21 2346078, E-mail: kafil.mahmood@tyndall.ie.

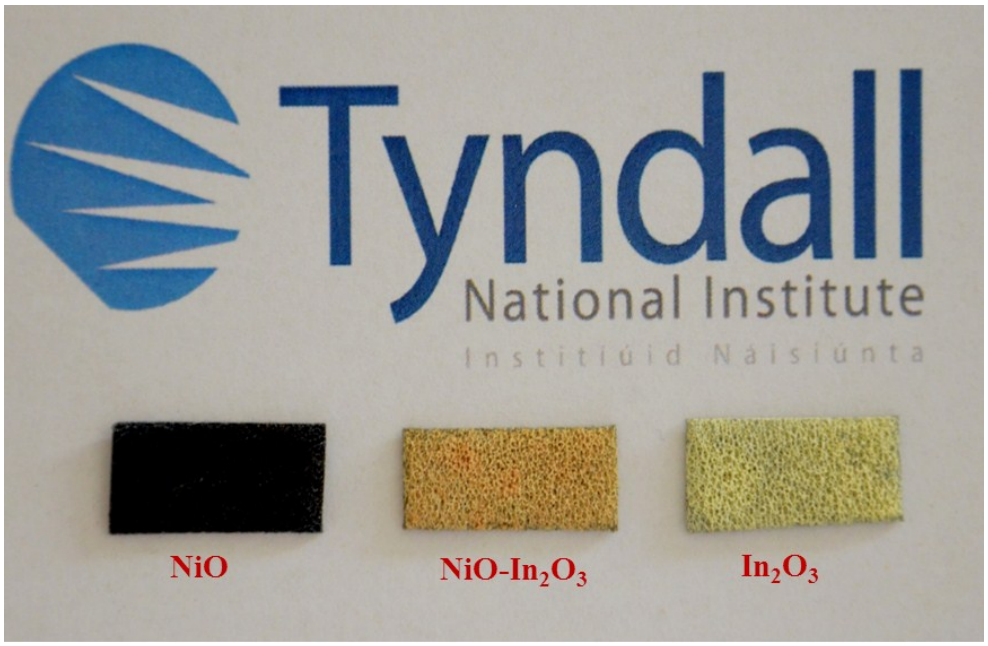

Fig. S1 Digital photograph of NiO, NiO-In_2O_3 (1:2) and In_2O_3 grown on NF substrate.

SI 1: SEM analysis of the NiO-In_2O_3-NF hybrid structure

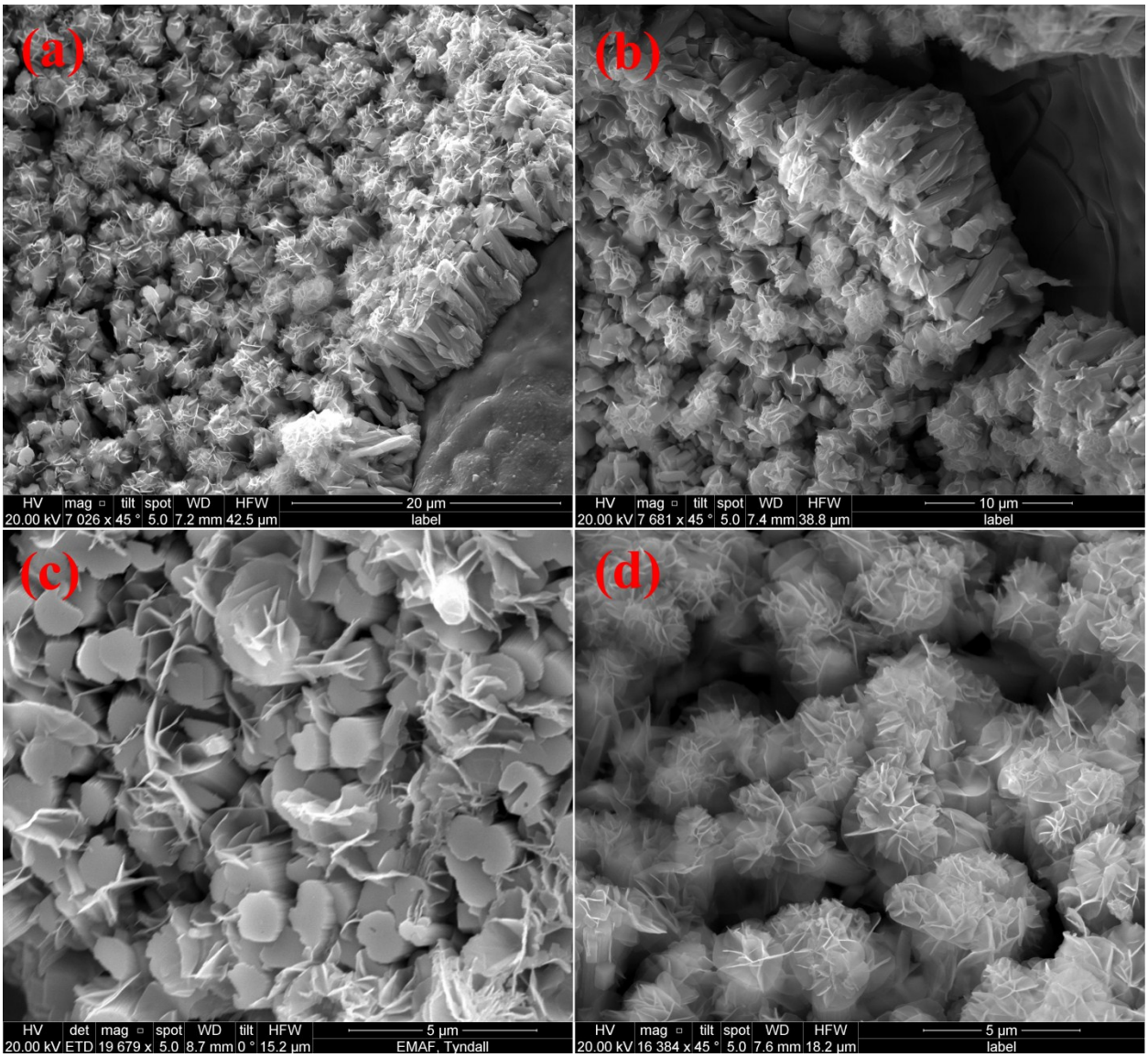

Fig. S2 (a-d) 45° tilted angle SEM images of NiO-In_2O_3-NF (1:2) hybrid structure.

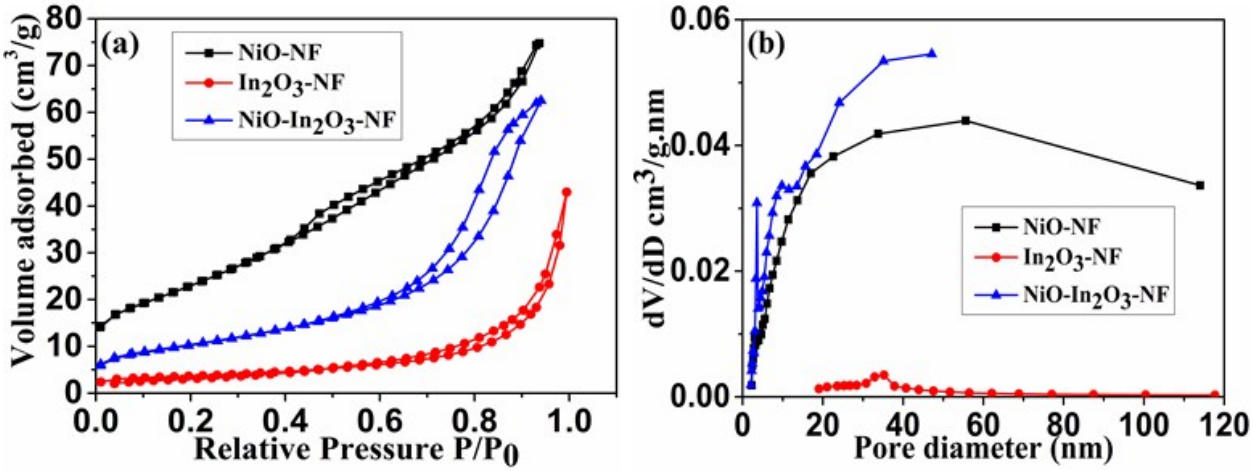

Fig. S3 (a) N_2 adsorption/desorption isotherms and (b) the corresponding pore size distribution curves of NiO-NF, In_2O_3-NF and NiO-In_2O_3-NF (1:2) electrode materials.

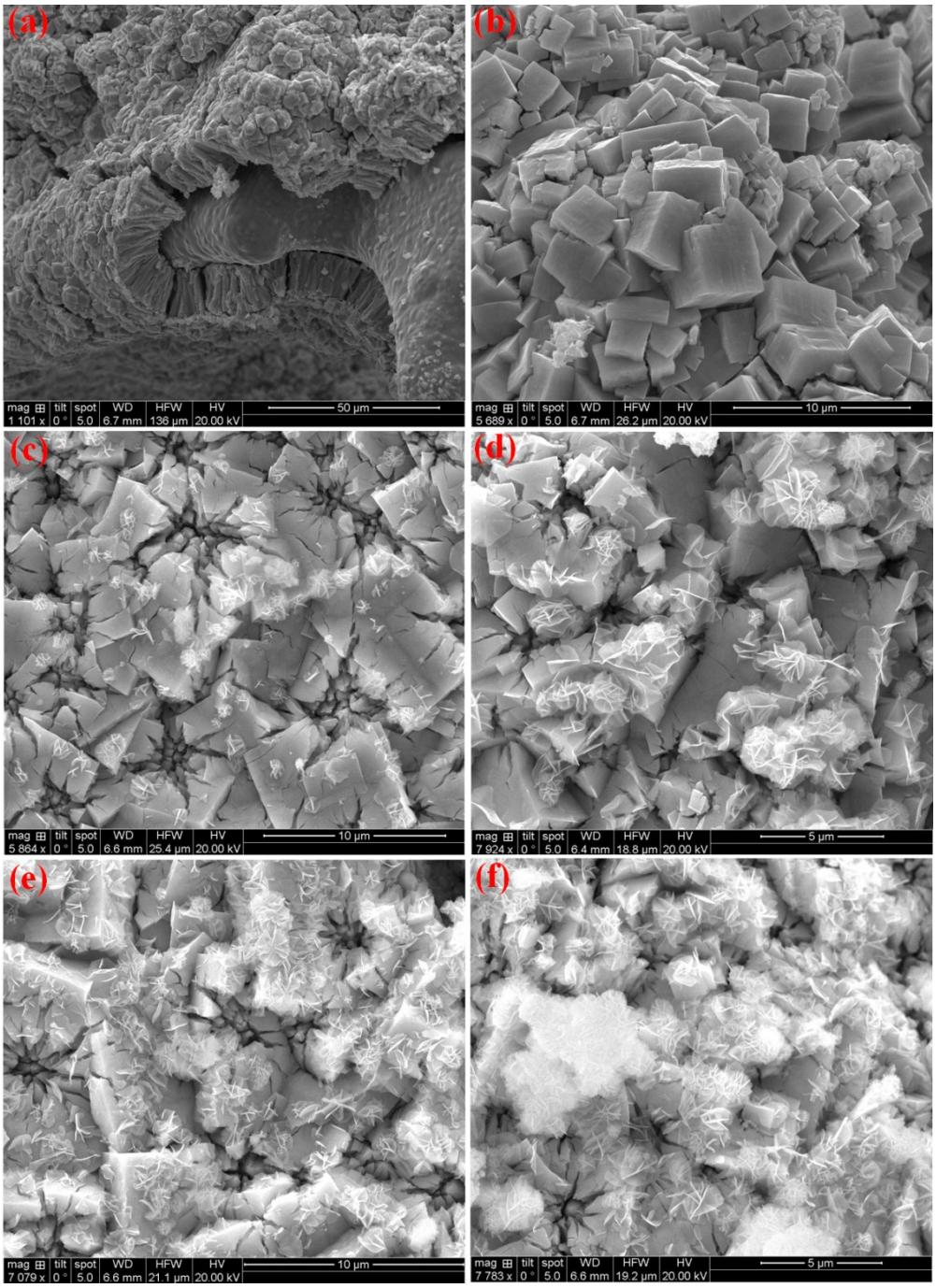

Fig. S4 (a-f) SEM images of NiO-In_2O_3-NF (1:2) hybrid structure captured at different time of growth 3 h (a & b), 6 h (c & d) and 9 h (e & f).

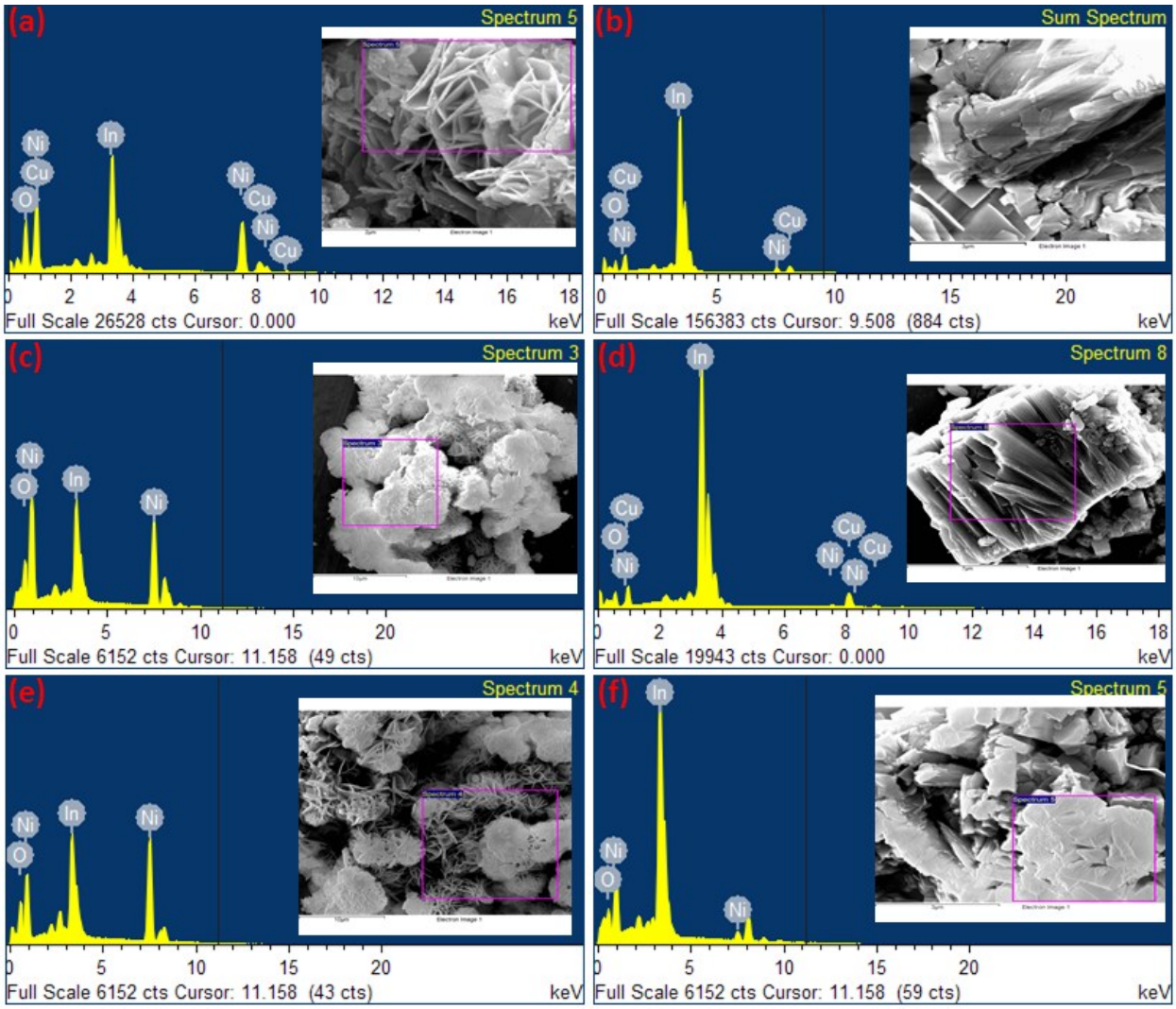

Fig. S5 EDX spectrum of NiO-In_2O_3-NF hybrid composite at various concentration of Ni:In (a and b) 1:1, (c and d) 1:2, and (e and f) 2:1 scanned at different regions. The observed Cu peak was due to the copper tape used to attach the samples to the sample holder.

SI 2: Growth process of the heterostructure

The growth process for this hybrid microstructure can be explained by the following chemical processes:

$(NH_2)_2$ (excess) + $nH_2O \rightarrow nNH_4OH + CO_2\uparrow$ (1)

nNH_4OH (excess) $\rightarrow nNH_4^+ + nOH^-$ (2)

$2In^{3+} + 6OH^- \rightarrow 2In(OH)_3 \rightarrow In_2O_3 + 3H_2O$ (3)

$Ni^{2+} + 2OH^- \rightarrow Ni(OH)_2 \rightarrow NiO + H_2O$ (4)

Generally, the hierarchical nanostructure can be grown under the surfactant mediated experimental conditions and the oriented attaching growth might be used to explain the formation mechanism.[1] Since the absence of surfactant during our synthesis, we propose the Oswald ripening mechanism for this anisotropic growth of hybrid structure.[1] In our study, water/ethanol mixed solvent and urea plays an important role in the formation of this hybrid microflower structure. It is reported that the polarity of the solvents can affect the dispersity of the reactants in the reaction medium, the nucleus formation in the products and their growth directions. Since the solvents are of different polarities, the less polar solvent could act as a surfactant over the metal-hydroxide surface and leads to the further particle assembly and their growth.[2] First, the hydrolysis of urea under mild (120 °C) hydrothermal condition, slowly produces the OH^- ions in the reaction system.[3,4] The slow reaction rates lead to the low degree of supersaturation in solution and eventually the nucleation between metal (In^{3+} and Ni^{2+}) and OH^- ions occurs. In our case, the nucleation occurs heterogeneously and forms the hybrid microstructure at the end.[4-6] To investigate this heterogeneous growth, pure NiO, In_2O_3 and various composition of NiO-In_2O_3 such as 1:1, 1:2 and 2:1 (Ni:In) have been grown over nickel foam under same experimental conditions. Also, time dependent experiments were carried out for 1:2 (Ni:In) composition. The SEM images of the samples are shown in Fig. S6(a-d) and Fig. S7(a-i) (SI). It shows the networked nanosheets like microstructure for pure NiO (Fig. S6(a and b)) and irregular aggregated nanocubes for pristine In_2O_3 (Fig. S6(c and d)). Ultimately, all the Ni-In mixed composites exhibited the hybrid microstructure as shown in Fig. S7(a-i) indicating the

heterogeneous growth of NiO-In_2O_3 mixed oxide. These results were in good agreement with the time dependent experiments as discussed earlier in the main text.

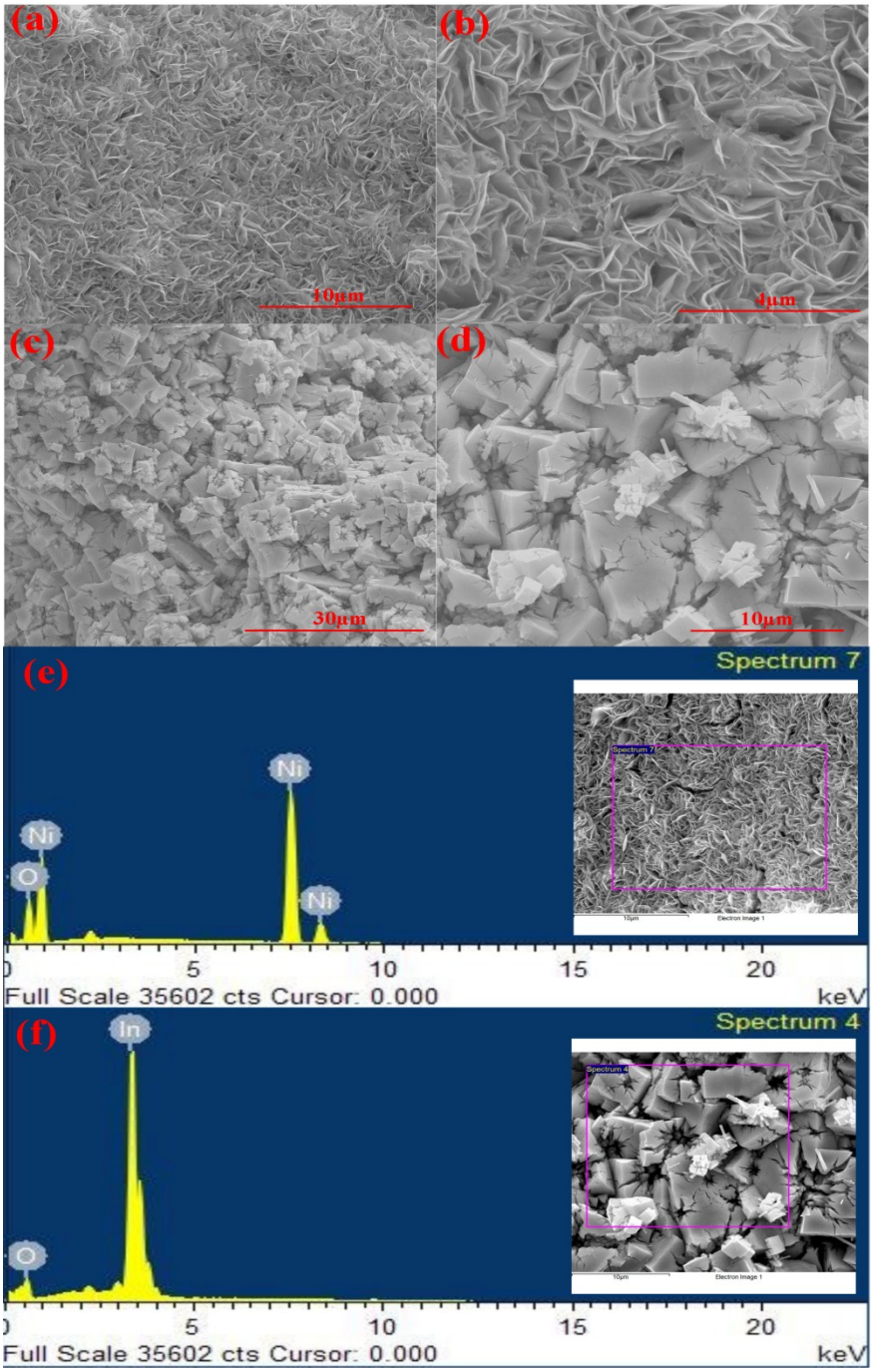

Fig. S6 SEM images of pure NiO-NF (a and b) and pure In_2O_3-NF (c and d). EDX spectrum of (e) pure NiO-NF and (f) Pure In_2O_3-NF.

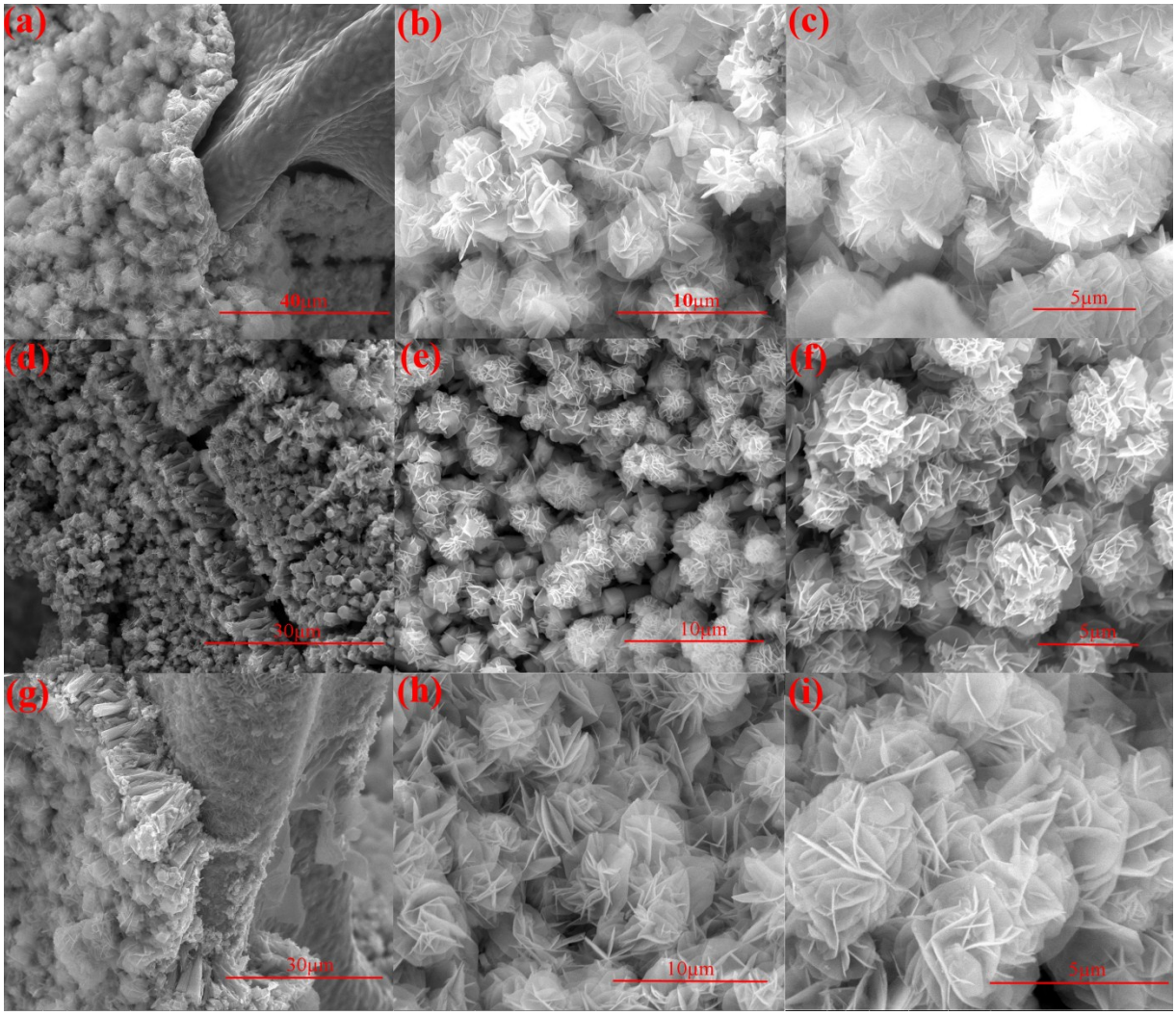

Fig. S7 (a-i) SEM images of NiO-In_2O_3-NF composites at various concentration of Ni and In, (a-c) 1:1, (d-f) 1:2 and (g-i) 2:1 at different magnifications.

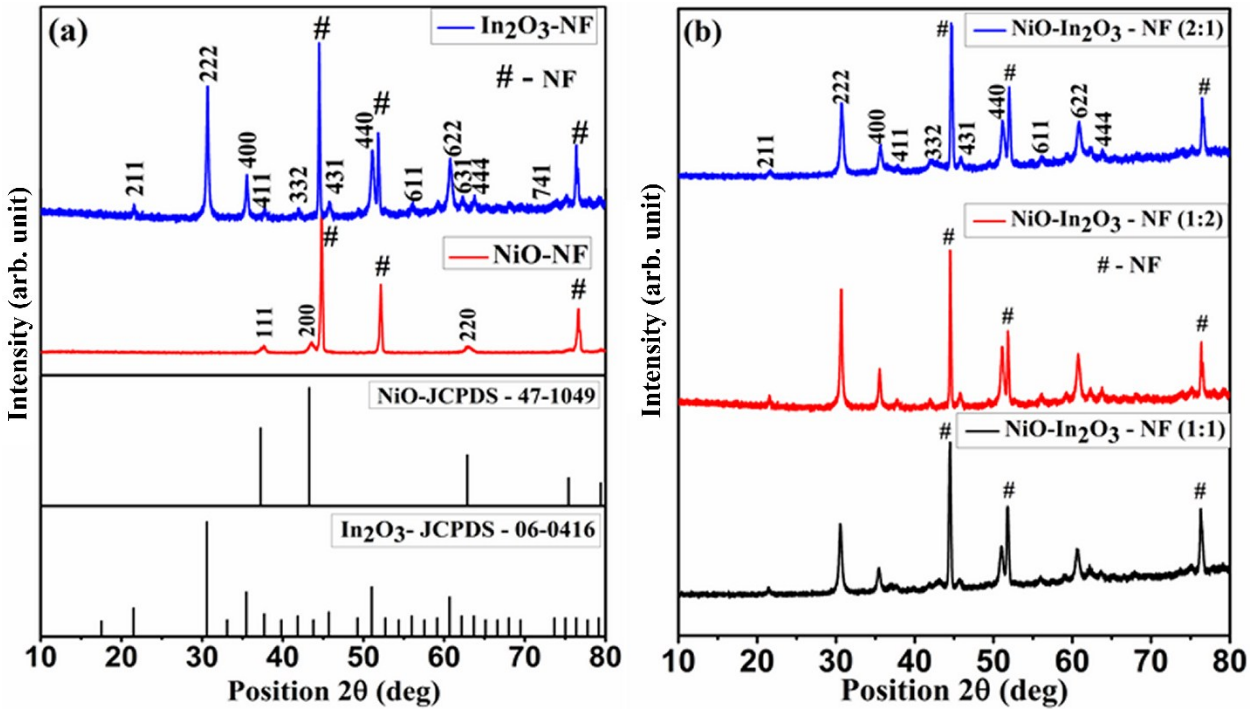

Fig. S8 (a) XRD pattern of pure NiO-NF and In_2O_3-NF with their stand JCPDS patterns and (b) XRD pattern of NiO-In_2O_3-NF composites prepared using different Ni/In concentrations.

SI 3: Raman Analysis

It is well recognized that Raman spectroscopy as a powerful tool to ascertain the secondary phases in the composites. Fig. S9 shows the Raman spectra of NiO-NF, In_2O_3-NF and NiO-In_2O_3-NF with different compositions. In the Raman spectra of NiO-NF sample, NiO shows two broad absorption bands at ~500 cm^{-1} and 1060 cm^{-1} correspond to the Ni-O stretching.[7] Similarly, the In_2O_3-NF shows the vibrational modes at 131, 306, 367, 497 and 630 cm^{-1}, associated to the vibrations of body centred cubic In_2O_3 structure.[8] In the NiO-In_2O_3-NF mixed oxides, a considerable variation in the peak positions is observed, especially the frequency region around 450-650 cm^{-1} (marked as a circle in Fig S9) compared to their mono-metallic oxides. These peak-shifts are due to the interaction between NiO and In_2O_3. Also, the peaks due to the Ni-O stretching at 557 cm^{-1} and 1060 cm^{-1} in the mixed oxide further confirm the formation NiO-In_2O_3 nanocomposite.

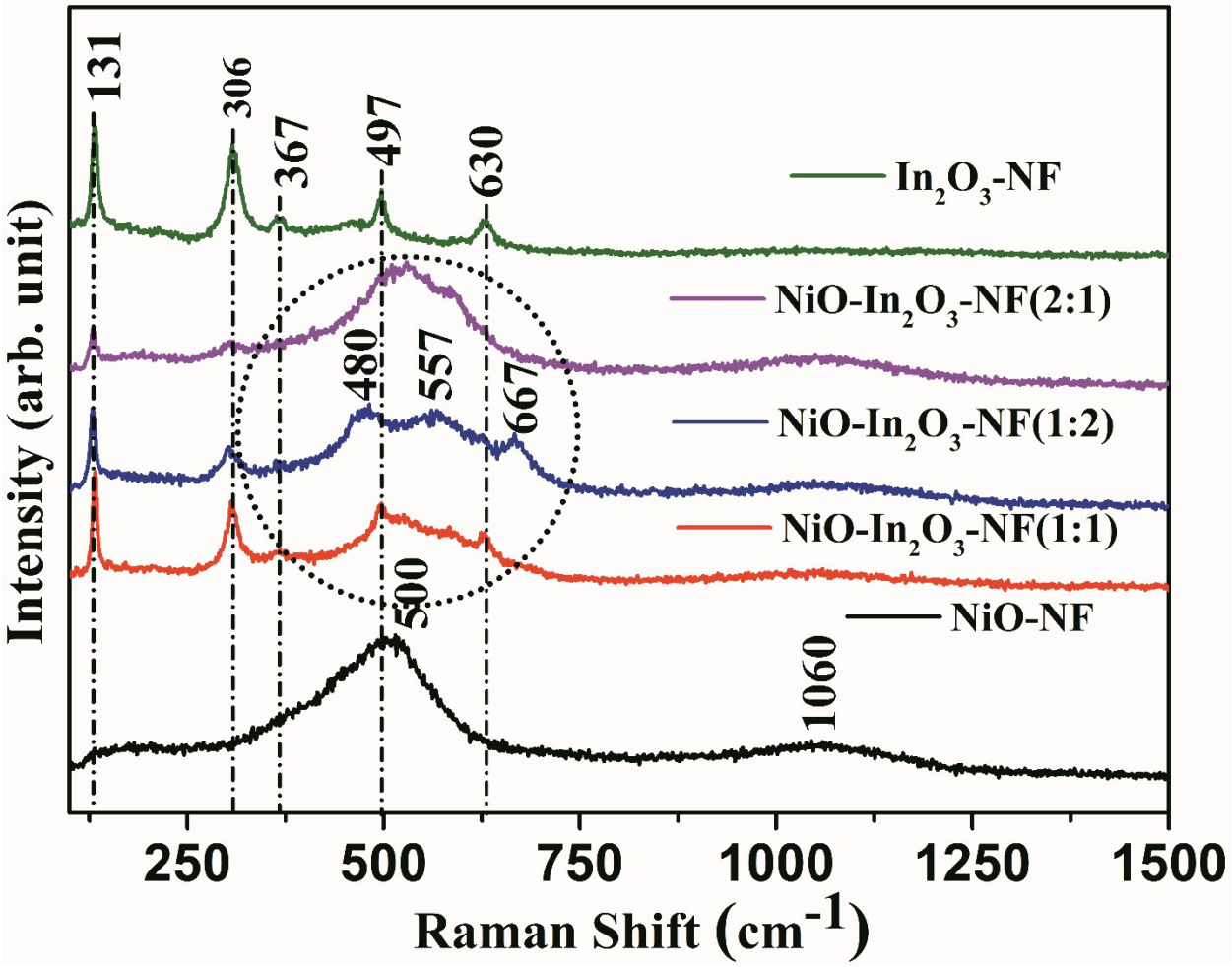

Fig. S9 Raman spectra of pure NiO-NF, In_2O_3-NF and NiO-In_2O_3-NF composites with different concentrations.

The equal molar concentration of Ni/In shows both the Ni-O and In-O-In stretching. Followed by the high Ni and low In concentration (Ni:In/2:1) shows predominant Ni-O vibrations in addition to the In-O-In stretching. However, the exact phase of the Ni compound is still unpredictable and can be attributed to the existence of low crystalline structure with many defects.

Table.1 Variation of elemental composition with respect to the NiO and In_2O_3 concentration. The observed Cu was due to the copper tape used to attach the samples to the sample holder.

Composition	Element/ Portion	Ni At%	In At%	O At%	Cu At%
NiO	Flakes	53.58	-	46.42	-
In_2O_3	Cubes	-	35.69	64.31	-
NiO-In_2O_3(1:1)	Rods	3.46	33.38	57.95	5.21
	Flowers	16.86	12.07	67.01	12.07
NiO-In_2O_3(1:2)	Rods	0.82	37.48	53.71	8.00
	Flowers	23.76	10.29	60.16	5.80
NiO-In_2O_3(2:1)	Rods	2.55	26.19	71.26	-
	Flowers	28.62	10.86	60.52	-

SI 4: XPS analysis of NiO and In_2O_3

The Ni2p, In3d and O1s XPS spectra of pure and NiO - In_2O_3 mixed oxides are shown in Fig. S10(a-c). The Ni2p spectrum of NiO shows the asymmetric main and multiplet-split $Ni2p_{3/2}$ (NiO) peaks at the corresponding binding energies of 853.8 (Ni^{2+}) and 855.9 (Ni^{3+}) eV, respectively. The satellite peaks in the respective binding energies further confirm the existence of Ni^{2+}/Ni^{3+} in the NiO sample.[9,10-12]The slight deviation in the peaks position from the binding energy value of pure NiO (854.2) is mainly attributed to the oxygen defects on the NiO surface.[13] The observed O1s spectrum (Fig. S10(c)) further proves this speculation. It shows a distinct peak at 529.3 eV and the shoulders at 531 and 532.5 eV related to the oxygen ions in the NiO crystal lattice and defects sites within the oxide crystals such as adsorbed oxygen (O_x^-) or hydroxide species.[13,14] Similarly, the pure In_2O_3 (Fig. S10(b)) show the dominant bands related to $In3d_{5/2}$ and $In3d_{3/2}$ at the binding energies of 444.5 eV and 452 eV, respectively. The existence of symmetric peaks indicates the oxidation state of In, rather than the metallic state. The strong O1s peak at 529.8 eV with a shoulder peak at 531.6 eV reveals the existence of In-O bonding with some adsorbed surface oxygen defects. The observed binding energies are in good agreement with earlier reports for In_2O_3 nanostructures (443.9 eV & 443.8 eV).[6, 12, 15, 16]

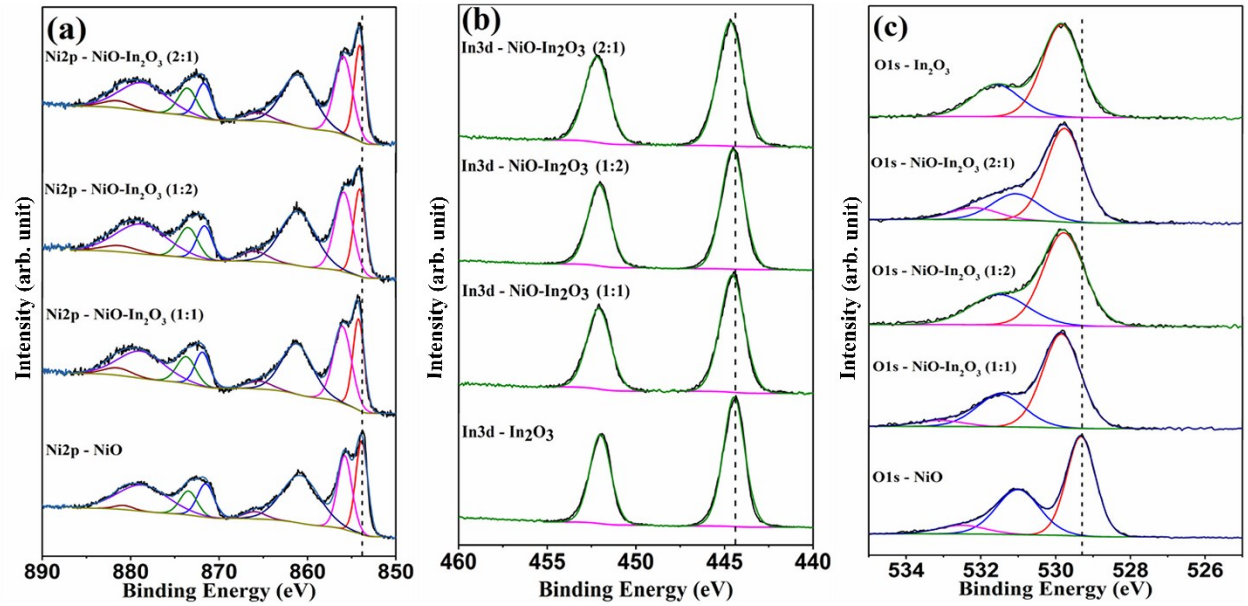

Fig. S10 (a-c) XPS spectra of pure andNiO-In_2O_3 hybrid structure prepared at various concentrations.

When compared to individual oxides, the XPS spectra of mixed compounds showed significant variations in the $Ni2p_{3/2}$ peak positions due to the addition of In_2O_3 as shown in Fig. S10(a). In particular, the intensity ratio of Ni^{2+}/Ni^{3+} has been varied according to the Ni:In concentrations. The NiO-In_2O_3 with equal concentration Ni:In(1:1) and Ni rich concentration Ni:In (2:1) showed the Ni^{2+}/Ni^{3+} intensity ratio of 0.62. Meantime, for the In rich NiO-In_2O_3 (1:2) hetero composite, the ratio was increased to 0.66 due to the high concentration of defects as supported by the Raman spectra. However, these values are quite lower than the pure NiO sample (0.84), which may be due to the decrease in hole concentration of p-type NiO semiconductors as a results of In incorporation.[9] This indicates that a limited amount of the In ions were incorporated into NiO lattice for all the composites. Similarly, the In3d spectra of NiO-In_2O_3 hetero-composites (Fig.S10(b)) showed the characteristic spin-orbit splits at the binding energies ranging from 444.4-444.7 eV and 452-452.2 eV corresponds to the $In3d_{5/2}$ and $In3d_{3/2}$, respectively.[9, 13-15] This indicated that element indium in NiO-In_2O_3 hetero-structures existed in the oxide state only.[15] The relation between metal and oxygen is further evaluated by the O1s XPS spectral analysis and depicted in Fig. S10(c) for the pure and NiO-In_2O_3 (1:1), NiO-In_2O_3 (1:2) and NiO-In_2O_3 (2:1) samples. Typical O1s spectra of all the

composites showed a distinct peak at 529.8±0.1 eV associated to the O^{2-} species in Ni-O and In-O. Also, there is a visible shoulder peaks between 531.1-532.2 eV and can be proposed to the defects sites within oxide crystal in addition to the adsorbed oxygen and hydroxides.[12] The ratio of the shoulder peak versus the total O1s peak for NiO:In_2O_3 composites are found to be 28.5%, 30.6% and 23.6% for Ni:In (1:1), Ni:In (1:2) and Ni:In (2:1) respectively, confirming the existence of more surface defects in Ni:In (1:2) sample than the other two compositions. These results are in good agreement with the observed Ni2p and In3d spectra as well as with the XRD and Raman analysis and contribute to our perception of the heterostructured composite, which is composed of NiO and In_2O_3.

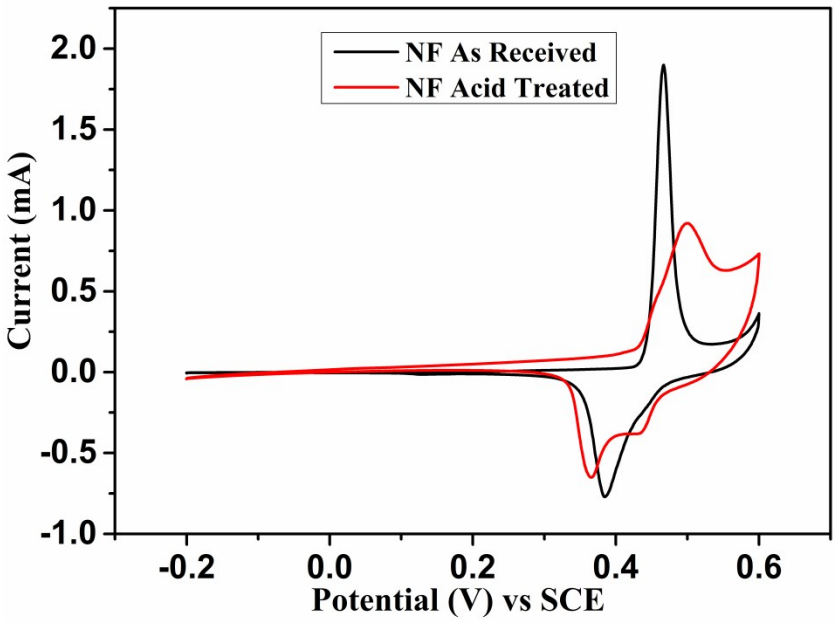

Fig. S11 CV curves of bare NF before (black) and after (red) acid treatment measured at 10 mV s^{-1}.

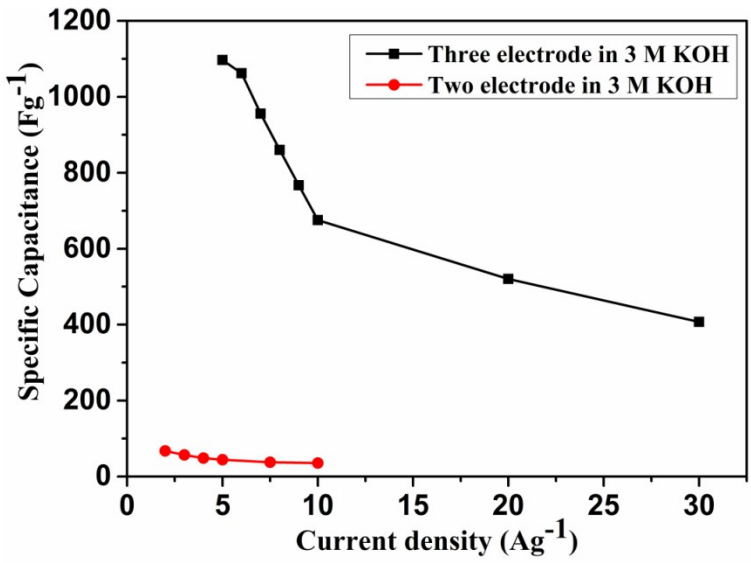

Fig. S12 Variation of specific capacitance with respect current density for NiO-In_2O_3-NF (1:2) hybrid electrode in both three and two electrode configurations.

Table 2. Comparison of electrochemical performance for different hetero-composite electrodes in three electrode configuration**.**

Materials	Specific Capacitance(Fg^{-1})	Current Density	Potential Window (V)	Cyclic Stability
$ZnO@MnO_2$[17]	423.5	0.5 Ag^{-1}	1	90.5% after 3000 cycles
$Mn_3O_4@PbO_2$[18]	338	10 $mAcm^{-2}$	~2.5	-
$CuO@MnO_2$[19]	167.2	0.3 Ag^{-1}	1	88.6% after 5000 cycles
$WO_3@MnO_2$[20]	363	0.5 Ag^{-1}	1	93.8% after 5000 cycles
$ZnO@Co_3O_4$[21]	857.7	2 $mAcm^{-2}$	0.5	96.8% after 6000 cycles
$TiO_2@Co(OH)_2$[22]	199 $mFcm^{-2}$	0.2 $mAcm^{-2}$	0.6	82.5% after 4000 cycles
$ZnO@Ni_3S_2$[23]	1529	2 Ag^{-1}	0.5	42% after 2000 cycles
$NiCo_2O_4@Ni_3S_2$[24]	1716	1 Ag^{-1}	0.6	83.7% after 2000 cycles
$Ni_3S_2@MoS_2$[25]	848	5 Ag^{-1}	0.8	91% after 2000 cycles
$Ni@Ni_3S_2$[26]	1293	5 Ag^{-1}	0.5	69% after 1000 cycles
$ZnO@Ni(OH)_2$[27]	2028	10 Ag^{-1}	0.5	68% after 500 cycles
CuO@NiO[28]	296.2	10 mVs^{-1}	0.6	97% after 500 cycles
$Ni(OH)@Fe_2O_3$[29]	908	21.8 Ag^{-1}	0.6	85.7% after 5000 cycles
$ZnO@MoO_3$[30]	241	5 mVs^{-1}	1.5	89.7% after 100 cycles
$NiO-In_2O_3$-NF	**1096.8**	**5 Ag^{-1}**	**0.75**	**89.5% after 5000 cycle (This Work)**

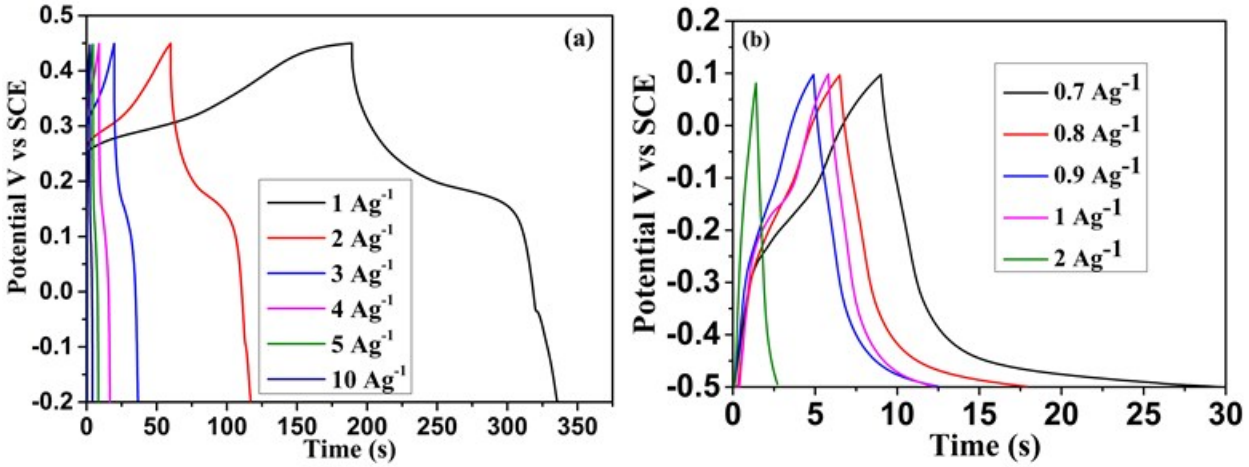

Fig. S13 Charge-discharge curves of (a) NiO-NF and (b) In_2O_3-NF at various current densities.

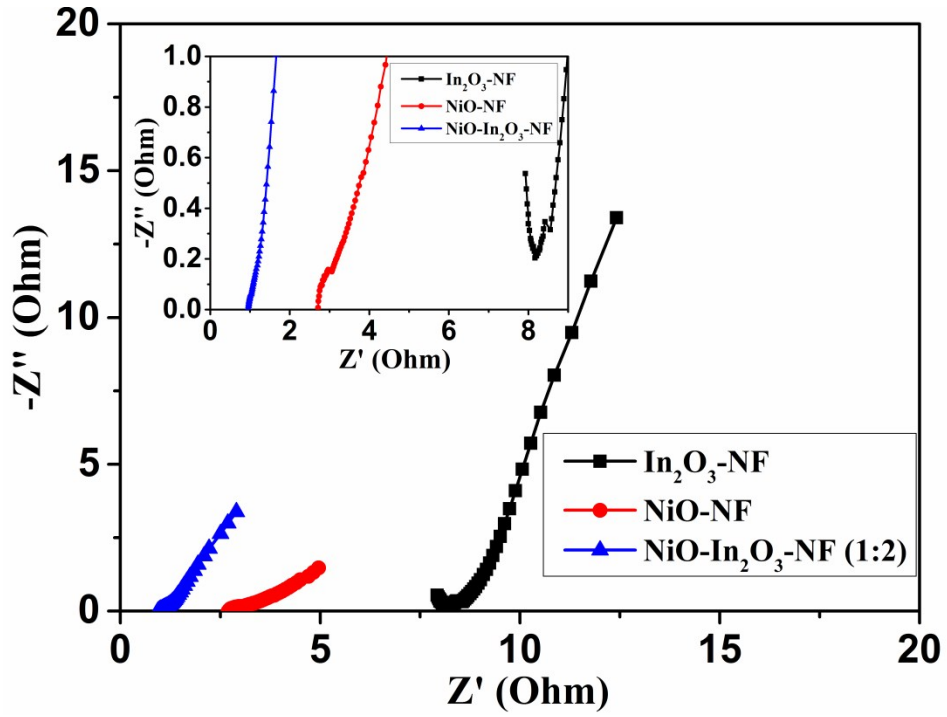

Fig. S14 Nyquist plot of In_2O_3-NF, NiO-NF and NiO-In_2O_3-NF electrode measured at 3 M KOH in three electrode configuration.

SI 5: Charge-discharge studies of NiO-In_2O_3 (1:1) and NiO-In_2O_3 (2:1) composites

The electrochemical performance of NiO-In_2O_3-NF (1:1) and NiO-In_2O_3-NF (2:1) were also measured using 3 M KOH electrolyte. Typical charge-discharge curves of the samples measured at different current densities are shown in Fig S15(a and b). Non-linear charge-discharge profile indicates the pseudocapacitive behaviour of the electrodes. However, the rate performance and specific capacitances were drastically varied when compared to the NiO-In_2O_3-NF(1:2) electrode. This may be due to the detachment of NiO from the In_2O_3 surface during electrochemical reactions owing to their inadequate hybridization and microstructure. The observed large IR drop during discharge in positive potential (i.e. active potential region of NiO ~ 0.5 to -0.2 V) in Fig. S15(a) further reveals the dis-integration of NiO. The specific capacitance values for these composites are found to be 404.1 Cg^{-1} (538.8 Fg^{-1}) for NiO-In_2O_3-NF (1:1) and 203.1 Cg^{-1} (270.8 Fg^{-1}) for NiO-In_2O_3-NF (2:1) at 5 Ag^{-1}, which are quite low than the NiO-In_2O_3-NF(1:2) electrode at the same current density. In case of NiO-In_2O_3-NF (2:1), the electron kinetics between NiO and In_2O_3 is not sufficient enough for complete utilization of NiO active sites. This is due to the formation of more $Ni^{3+}O_x$ phase via the adsorption of negatively charged oxygen on the NiO surface as evidenced from the XPS analysis.[9] Thereby, only part of the NiO has been involved to redox process, resulting low specific capacitance.

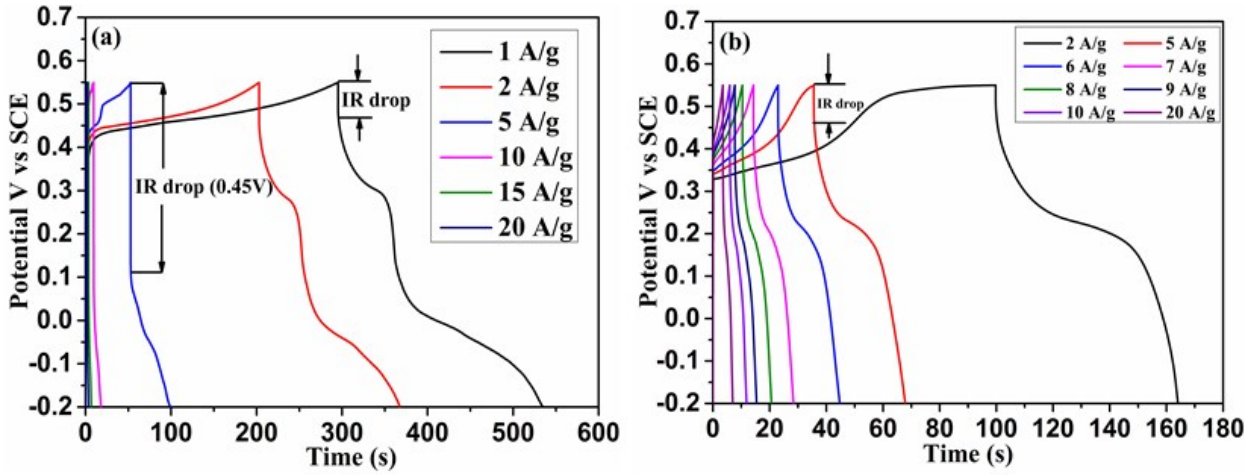

Fig. S15 Charge-discharge curves of (a) NiO-In_2O_3-NF (1:1) composite and (b) NiO-In_2O_3-NF (2:1) composite at various current densities.

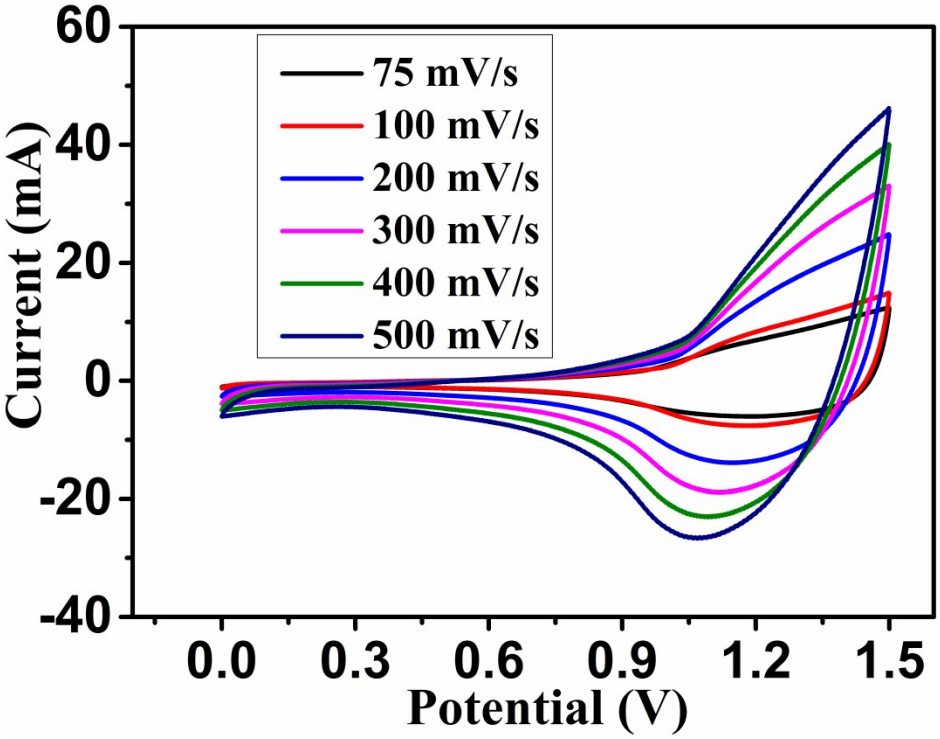

Fig. S16 Cyclic voltammograms of NiO-In_2O_3-NF (1:2) based symmetric supercapacitor at high scan rates.

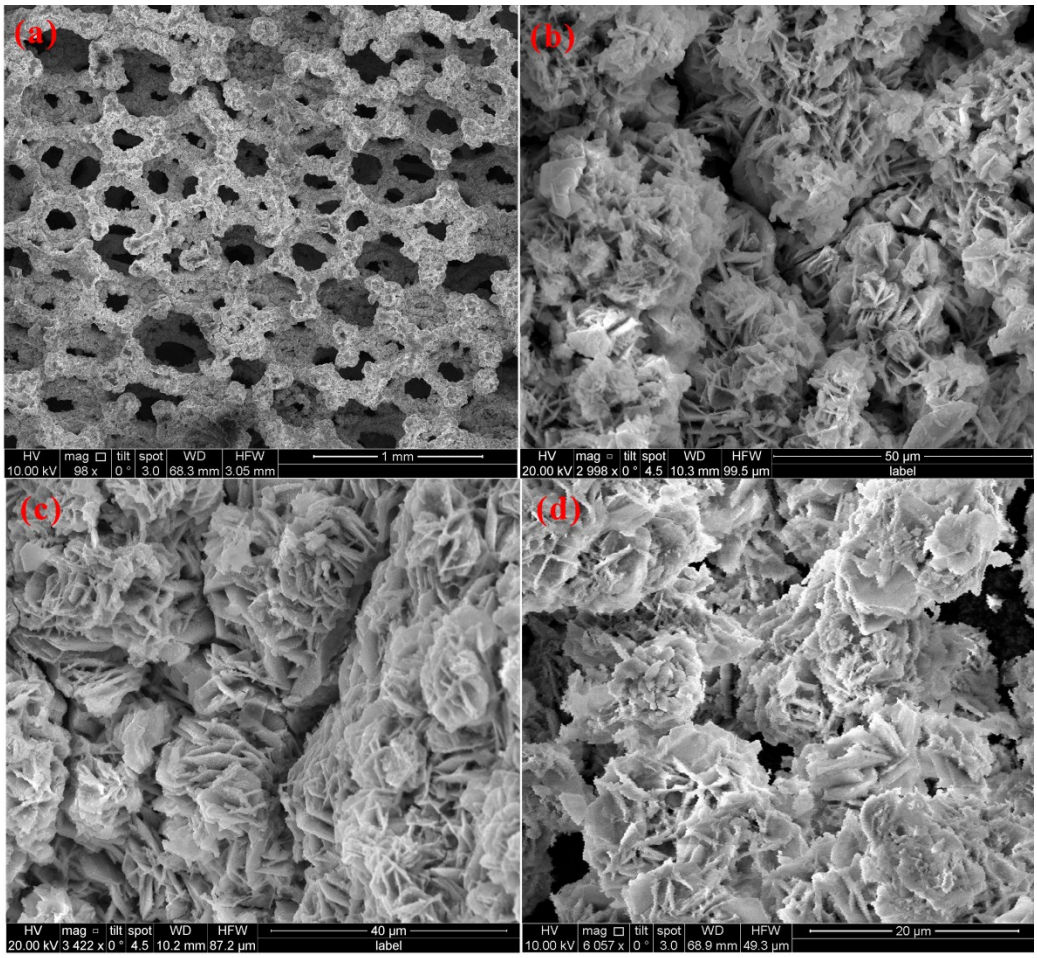

Fig. S17 (a-d) SEM images of NiO-In_2O_3-NF (1:2) electrode after 50,000 charge-discharge cycles.

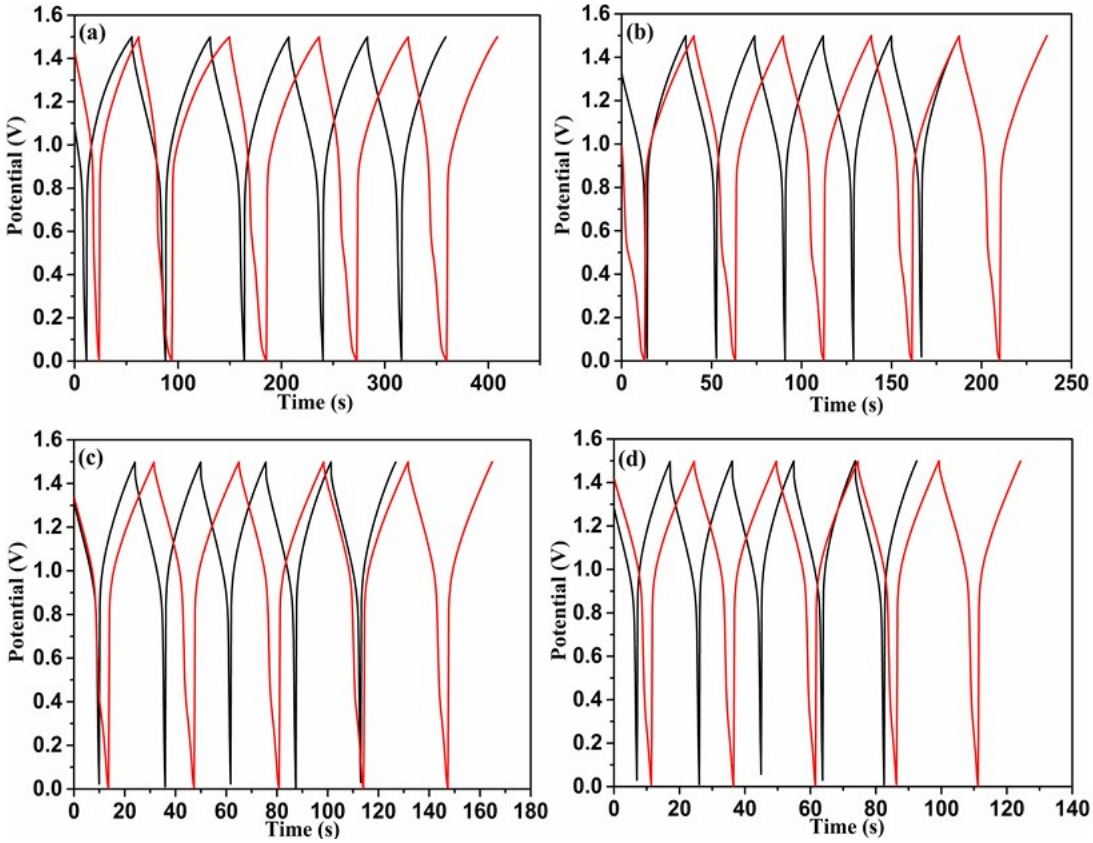

Fig. S18 First few charge-discharge cycles of NiO-In_2O_3-NF (1:2) based symmetric supercapacitor measured before (black line) and after (red line) 1000 cycles at different current density (a) 2 A/g, (b) 4 A/g, (c) 6 A/g and (d) 8 A/g.

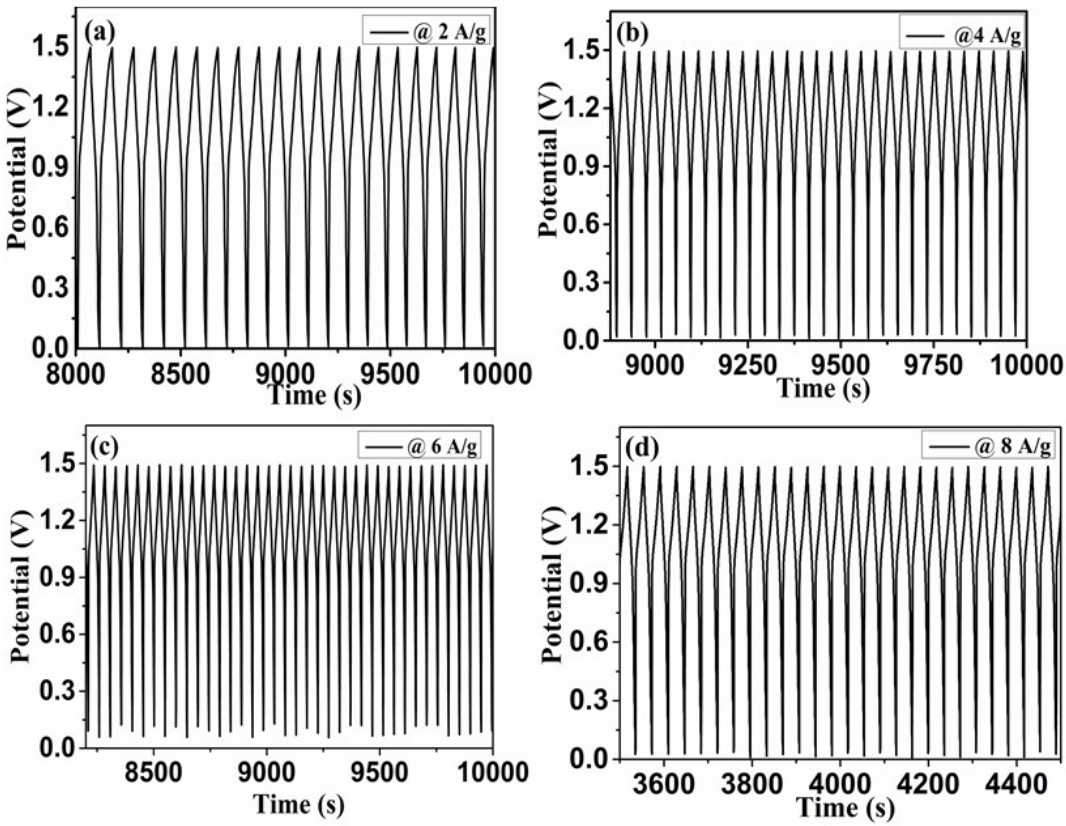

Fig. S19 Continuous charge-discharge cycles of NiO-In_2O_3-NF (1:2) based symmetric supercapacitor measured at different current densities.

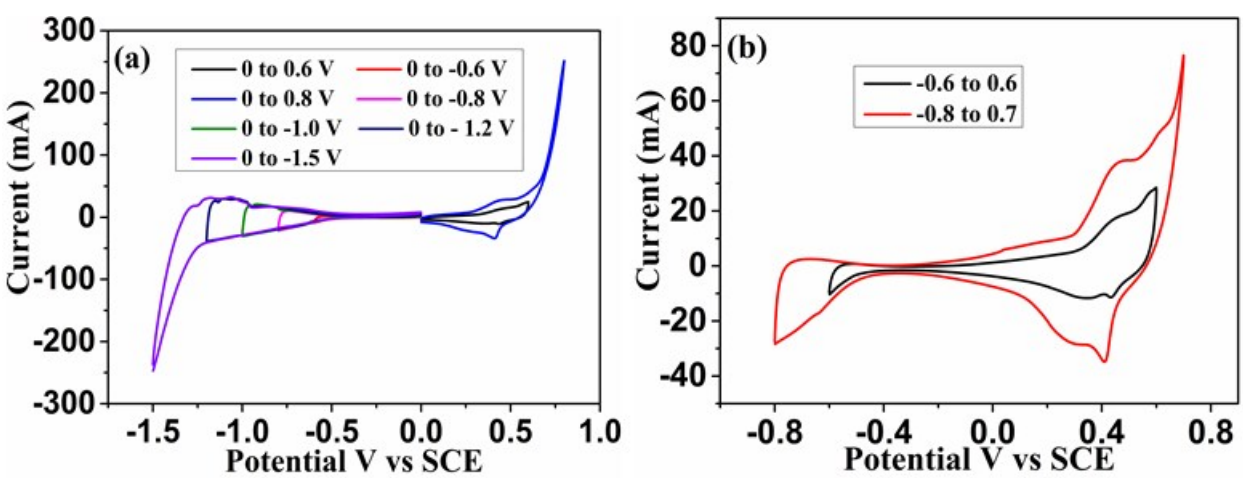

Fig. S20 (a) Cyclic voltammograms of NiO-In_2O_3-NF symmetric cell at different potential range and (b) the stable potential window of the device with respect to reference electrode.

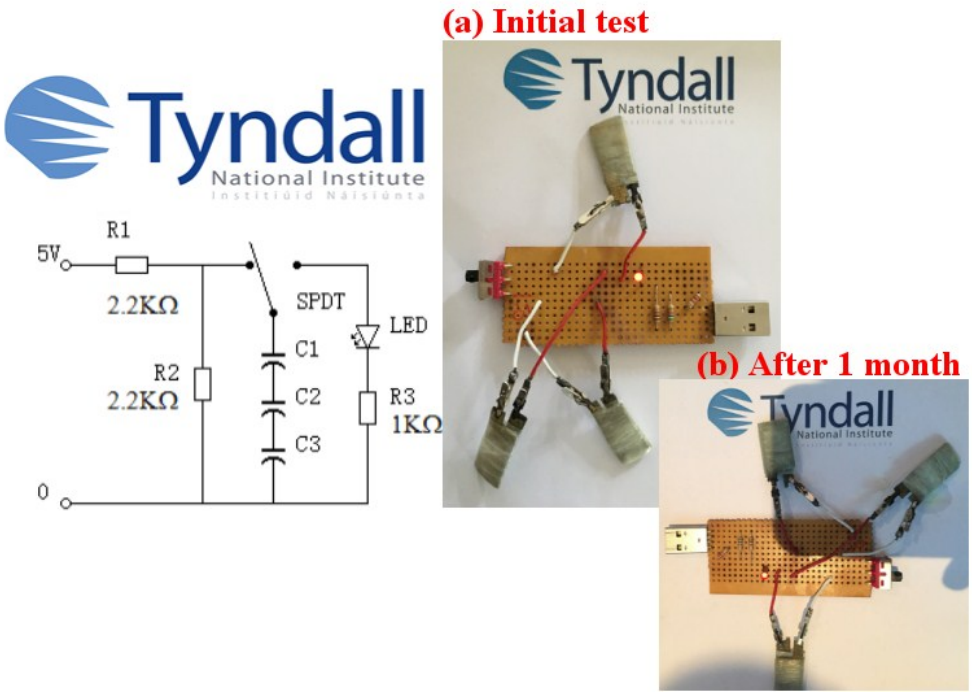

Fig. S21 NiO-In_2O_3-NF (1:2) based symmetric supercapacitor connected in series and their practical application of LED lighting.

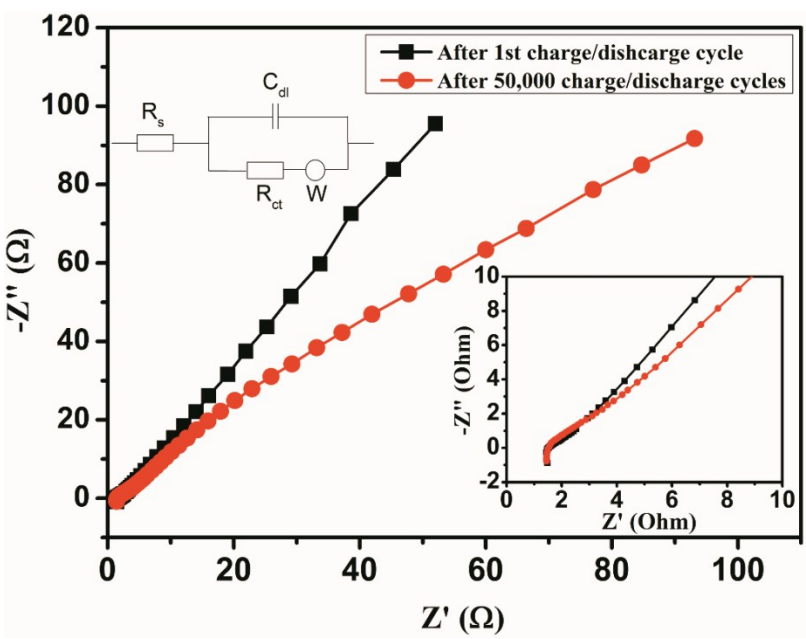

Fig. S22 Nyquist plot for NiO-In_2O_3-NF (1:2) based symmetric supercapacitor before and after 50,000 cycles. Inset on the left is the equivalent circuit and inset on the right is showing the expanded view of the high frequency region.

References

1 J. Liu, T. Luo, F. Meng, K. Qian, Y. Wan, J. Liu, *J. Phys. Chem., C* 2010, **114**, 4887.

2 H. Du, L. Jiao, K. Cao, Y. Wang, H. Yuan, *ACS Appl. Mater. Interfaces.,* 2013, **5**, 6643.

3 N. Padmanathan, S. Selladurai, *RSC Adv.,* 2014, **4**, 8341.

4 Y. Ren, L. Gao, *J. Am. Ceram. Soc.* **2010**, 93, 3560.

5 K. H. Hsua, K. S. Chen, *Ceramics International,* 2000, **26**, 469.

6 W. Tian, X. Wang, C. Zhi, T. Zhai, D. Liu, C. Zhang, D. Golberg, Y. Bando, *Nano Energy,* 2013, **2**, 754.

7 C. Luo, D. Li, W. Wu, Y. Zhang, C. Pan, *RSC Adv.,* 2014, **4**, 3090.

8 G. Mohan Kumar, A. Madhan Kumar, P. Ilanchezhiyan, T. W. Kang, *Nanoscale,* 2014, **6**, 11226.

9 H. J. Kim, H. M. Jeong, T. H. Kim, J. H. Chung, Y. C. Kang, J. H. Lee, *ACS Appl. Mater. Interfaces,* 2014, **6**, 18197.

10 F. Lin, D. Nordlund, T. C. Weng, R. G. Moore, D. T. Gillaspie, A. C. Dillon, R. M. Richards, C. Engtrakul, *ACS Appl. Mater. Interfaces,* 2013, **5**, 301.

11 C. Dong, Q. Li, G. Chen, X. Xiao, Y. Wang, *Sensors and Actuators B,* 2015, **220**, 171.

12 B. Zhao, X. K. Ke, J. H. Bao, C. L. Wang, L. Dong, Y. W. Chen, H. L. Chen, *J. Phys. Chem. C,* 2009, **113**, 14440.

13 W. J. Tseng, T. T. Tseng, H. M. Wu, Y. C. Her, T. J. Yang, *J. Am. Ceram. Soc.,* 2013, **96**, 719.

14 X. Meng, L. Tang, J. Li, *J. Phys. Chem. C,* 2010, **114**, 17569.

15 J. Mu, B. Chen, M. Zhang, Z. Guo, P. Zhang, Z. Zhang, Y. Sun, C. Shao, Y. Liu *ACS Appl. Mater. Interfaces,* 2012, **4**, 424.

16 X. Meng, L. Tang, J. Li, *J. Phys. Chem. C,* 2010, **114**, 17569.

17 M. Huang, F. Li, X. L. Zhao, D. Luo, X. Q. You, Y. X. Zhang, G. Li, *Electrochim. Acta,* 2015, **152**, 172.

18 Y. Dan, H. Lin, X. Liu, H. Lu, J. Zhao, Z. Shid, Y. Guo, *Electrochim. Acta,* 2012, **83**, 175.

19 Y. X. Zhang, F. Li, M. Huang, *Materials Letters* , 2013**, 112**, 203.

20 C. Yuan, H. Lin, H. Lu, E. Xing, Y. Zhang, B. Xie *Materials Letters,* 2015, **148**, 167.

21 D. Cai, H. Huang, D. Wang, B. Liu, L. Wang, Y. Liu, Q. Li, T. Wang, *ACS Appl. Mater. Interfaces,* 2014, **6**, 15905.

22 A. Ramadoss, S. J. Kim, *Electrochim. Acta,* 2014, **136**, 105.

23 Z. Xing, Q. Chu, X. Ren, C. Ge, A. H. Qusti, A. M. Asiri, A. O. Al-Youbi, X. Sun, *J. Power Sources,* 2014, **245**, 463.

24 J. Wang, S. Wang, Z. Huang, Y. Yu, *J. Mater. Chem. A*, 2014, **2**, 17595.

25 J. Wang, D. Chao, J. Liu, L. Li, L. Lai, J. Lin, Z. Shen, *Nano Energy*, 2014, **7**, 151.

26 K. Krishnamoorthy, G. K. Veerasubramani, S. Radhakrishnan, S. J. Kim, *Chemical Engineering Journal*, 2014, **251**, 116.

27 Z. Pu, Q. Liu, A. H. Qusti, A. M. Asiri, A. O. Al-Youbi, X. Sun, *Electrochim. Acta,* 2013, **109**, 252.

28 J. L. Yin, J. Y. Park, *Int. J. Hydrogen Energy,* 2014, **39**, 16562.

29 W. Tian, X. Wang, C. Zhi, T. Zhai, D. Liu, C. Zhang, D. Golberg, Y. Bando, *Nano Energy,* 2013, **2**, 754.

30 G. R. Li, Z. L. Wang, F. L. Zheng, Y. N. Ou, Y. X. Tong, *J. Mater. Chem.,* 2011, **21**, 4217.